

Enhanced Electroluminescence of Poly(2-methoxy-5-(2'-ethylhexyloxy)-1,4-phenylene vinylene) Films in the Presence of TiO₂ Nanocrystals

Chin-Cheng Weng¹, Chia-Hung Chou¹, Kung-Hwa Wei^{1,*} and Jung Y. Huang²

¹Department of Materials Science and Engineering, National Chiao Tung University, 1001 Ta Hsueh Road, Hsinchu 30050, Taiwan, Republic of China

²Department of Electro-Optical Engineering, National Chiao Tung University, 1001 Ta Hsueh Road, Hsinchu 30050, Taiwan, Republic of China

(*Author for correspondence; Tel.: +886-35-731871; Fax: +886-35-724727; E-mail: khwei@cc.nctu.edu.tw)

Received 4 February 2005; accepted in revised form 26 October 2005

Key words: TiO₂, Nanoneedles, Nanocomposites, Poly(2-methoxy-5-(2'-ethylhexyloxy)-1,4-phenylene vinylene)

Abstract

We demonstrated that in a nanocrystalline TiO₂/poly(2-methoxy-5-(2'-ethylhexyloxy)-1,4-phenylene vinylene) (MEH-PPV) composite, electroluminescence of this composite is enhanced via addition of TiO₂ nanoneedles. The TiO₂ nanoneedles enhance the partial crystallization of MEH-PPV around TiO₂, which in turn causes a decrease in the hole barrier height and an increase in hole mobility. The *I*-*V* measurement was established on an indium tin oxide/MEH-PPV:TiO₂/Al device to identify the electrical properties of the composites.

Introduction

In the past few decades, conjugated aromatic polymers have attracted considerable interest because of their diverse applications, ranging from electronic devices to light-emitting diodes and photovoltaic devices [1–9]. Although these polymers exhibit moderate photoluminescence (PL) quantum efficiencies and good thermal stabilities, their application in light-emitting diode devices is hampered by the formation of chain aggregates in the solid state [10]. Many studies have attempted to enhance the quantum efficiency by controlling the conjugation length [11, 12], blending with small organic molecules [13], changing the polymer structures to form asymmetric poly(this *p*-phenylene vinylene) derivatives [8], or using an electron-transporting layer [9]. The major approaches to improve the luminescent efficiency of polymers are attaching bulky side groups or silsesquioxane to the main-chain structures to alter the polymer interchain distance [14].

In recent years, greater interest has been directed toward the study of hybrid organic/inorganic nanostructures, owing to the possibility of combining the electrical properties of semiconducting organic polymers with the optical peculiarities of inorganic nanostructures like rods, particles, and thin films [15–30]. The energy transport and electron transport properties of these conjugated polymer/inorganic nanocrystals nanocomposites have been explored in several studies [20–28].

For instance, some studies report that luminescence from poly(2-methoxy-5-(2'-ethylhexyloxy)-1,4-phenylene vinyl-

ene) (MEH-PPV) can be quenched (for photovoltaic devices) or the energy can be transferred to the quantum dots [19–28]. TiO₂ nanocrystals blended with electroluminescent organics have shown lasing action with greatly reduced threshold pump powers [16, 21, 31]. Previous studies concerning TiO₂/MEH-PPV composites films indicated that their electroluminescence (EL) increases with the size of the TiO₂ nanoparticles in the range between 7 and 23 nm, and the crystal structure of TiO₂ also plays an important role [16, 17]. As compared with most conjugated polymer/inorganic nanocrystal composites, smaller inorganic nanocrystals such as quantum dots or rods (smaller than 10 nm) at the same loading generate more surface area for photogenerated electron transfer. In other words, the quenching effect of the luminescence will be reduced as the size of the incorporated inorganic crystals increases at the loading (total surface area decreases). This is one of the reasons for increasing EL efficiency in the TiO₂ particles/MEH-PPV studies [16, 17].

Here, we chose to blend rutile-phase TiO₂ nanoneedles with MEH-PPV. The rutile TiO₂ is a chemically stable material [32], and needlelike TiO₂ nanocrystals with a high aspect ratio could easily form a percolation network within MEH-PPV, which can influence the electron and hole transport in devices [33–35].

In the present study, we propose a new approach which blends needlelike TiO₂ nanostructures into MEH-PPV polymer in order to form a percolation network geometry. We investigate the effect of the addition of these TiO₂ nanoneedles on the electrical properties by *I*-*V* measurement.

Experimental

Materials

1,4-Bis(chloromethyl)-2-(2'-ethylhexyloxy)-5-methoxybenzene, 4-*tert*-butylbenzyl bromide, and potassium *tert*-butoxide (1.0 M solution in tetrahydrofuran, THF) were purchased from Aldrich and were used without further purification unless otherwise noted. THF was dried and purified by fractional distillation over sodium/benzophenone and was handled in a moisture-free atmosphere. Polystyrene-*block*-poly (4-vinylpyridine) (PS-*b*-P4VP) diblock copolymer was purchased from Polymer Source. The number-average molecular weights (M_n) of the PS and P4VP blocks for the first copolymer were 92,700 and 32,700, respectively, with the ratio of the weight-average molecular weight (M_w) to M_n (polydispersity) equal to 1.13, as determined by size-exclusion chromatography. Titanium oxide sulfate hydrate ($TiOSO_4 \cdot xH_2O$, Riedel-de Haën), urea (98%, Showa), Toluene (99% Tedia USA), and HCl (36% Acros) were used in the study.

Synthesis of MEH-PPV

A solution of 1.5 mL of potassium *tert*-butoxide (1.0 M THF solution, 1.5 mM) was slowly added to a stirred solution of 1,4-bis(chloromethyl)-2-(2'-ethylhexyloxy)-5-methoxybenzene (0.084 g, 0.25 mM) in 15 mL of dry THF and stirred for 1 h. A small amount of 4-*tert*-butylbenzyl bromide was added to the mixture to end-cap the polymer chain, with further stirring for 1 h. The polymerization solution was poured into 150 mL of methanol and the crude polymer was Soxhlet-extracted with methanol to remove the impurities and oligomers. The resulting polymer was redissolved in chloroform and reprecipitated into methanol. After filtration and drying under a vacuum, a bright-red polymer was obtained (yield 82%). The synthetic process is shown in Scheme 1.

A 1H -NMR spectrum of the polymer is shown in Figure 1. 1H NMR spectra were recorded using a Bruker DRX-300 spectrometer, and chemical shifts were measured in units of parts per million (ppm), with the residual proton solvent resonance as a reference (chloroform, 7.24 ppm). The spectrum shows a broad resonance between 7.8 and 7.4 ppm (aromatic protons), and peaks at 7.1 ppm (vinylic protons), 3.9 ppm (alkyl protons adjacent to the oxygen atom in the side chain), and between 2.0 and 0.7 ppm (other alkyl protons). Average molecular weights were

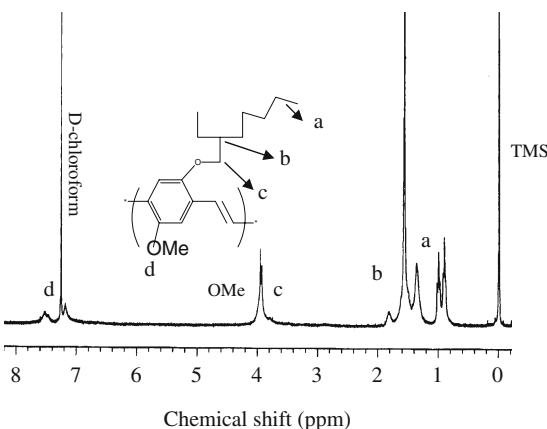


Figure 1. 1H -NMR spectrum of poly(2-methoxy-5-(2'-ethylhexyloxy)-1,4-phenylene vinylene) (MEH-PPV).

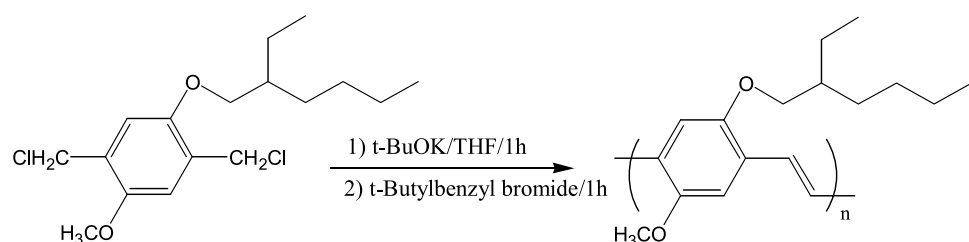
determined by means of gel-permeation chromatography (GPC) analysis on the basis of uniform PS standards, using THF as the solvent at a flow rate of 1 mL/min at 40 °C. GPC analysis was performed using a Waters 410 differential refractometer and a Waters 600 controller (Waters Styragel column). The measured values of M_n and M_w were 37,749 and 93,327, respectively, with a polydispersity of 2.47.

Preparation of TiO_2 nanoneedles and TiO_2 /MEH-PPV nanocomposites

The seeds used to grow TiO_2 nanoneedles were prepared using PS-*b*-P4VP as a template. The substrates with TiO_2 seeds were grown in TiO_2 precursor solutions with Ti concentrations of 0.0001–0.1 M at 85 °C to form TiO_2 nanoneedles. The detailed synthetic process was reported in our early study [36]. The needlelike TiO_2 nanostructures were collected from the grown substrate with ultrasonics in deionized water. After drying, the TiO_2 nanoneedles were then added to 1 wt% MEH-PPV in 1,2-dichloroethane solution and stirred for 24 h to form a homogeneous solution.

Characterization

Transmission electron microscopy (TEM) studies were carried out using a Hitachi H-600 electron microscope operating at 100 keV. High-resolution TEM (HRTEM) studies were carried out using a JEOL 2010 electron



Scheme 1. Synthesis of poly(2-methoxy-5-(2'-ethylhexyloxy)-1,4-phenylene vinylene).

microscope operating at 200 keV. An X-ray diffraction (XRD) study was carried out with a MAC Science MXP 18 X-ray diffractometer (50 kV, 200 mA) with a copper target and a nickel filter. The XRD profiles of powdered TiO_2 nanoneedles were collected at a scanning rate of $4^\circ/\text{min}$. The XRD profile of MEH-PPV and 5 wt% TiO_2 /MEH-PPV films which were cast at room temperature and then dried at 100°C in vacuum oven for 12 h to remove the solvent were collected at a scanning rate of $1^\circ/\text{min}$. The glass-transition temperatures of TiO_2 /MEH-PPV composites were obtained using a DuPont DSC 2910 at a heating rate of $20^\circ\text{C}/\text{min}$. The samples were dried at 100°C in a vacuum oven for 12 h to remove the solvent. The thermal gravimetric properties of MEH-PPV and TiO_2 /MEH-PPV were determined out with a Du Pont TGA 2950 at a heating rate of $20^\circ\text{C}/\text{min}$.

The current vs voltage ($I-V$) studies for TiO_2 /MEH-PPV solid films were carried out in a sandwich structure [Al/MEH-PPV: TiO_2 /indium tin oxide (ITO) glass]. The top Al electrode, with an area of 1.0 mm^2 , was deposited by thermal evaporation in a vacuum at $4 \times 10^{-6} \text{ Pa}$ on TiO_2 /MEH-PPV films, which had previously been spun and dried on ITO glass. These polymer films were dried at 100°C under vacuum for 12 h before evaporating the Al electrode. $I-V$ curves were obtained using a Keithley 237, a high-voltage-source measuring unit. The upper voltage and current limits of the Keithley 237 are 1,000 V and 10 mA.

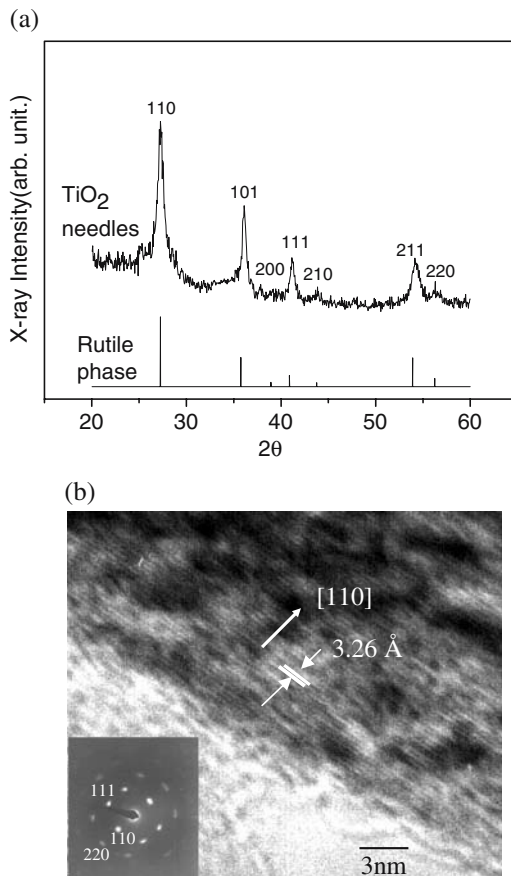


Figure 2. (a) X-ray diffraction curves of TiO_2 nanoneedles and (b) a high-resolution transmission electron microscopy (TEM) image of TiO_2 nanoneedles.

Cyclic voltammetry (CV) curves were measured by coating the polymer on a Pt plate and using a standard calomel electrode as the reference and 0.1 M $(n\text{-Bu})_4\text{NBF}_4$ /acetonitrile as the electrolyte. The scanning rate was set to 50 mV/s . The $I-V$ and EL measurements could be established stably for at least 5 times scans.

Results and discussion

Figure 2a shows an XRD pattern of the TiO_2 nanoneedles, which were harvested from a silicon wafer by ultrasonic vibration. These needlelike nanostructured TiO_2 nanoneedles exhibit a clearly tetragonal structure (rutile) by comparison with the JCPDS card file no. 75-1757 (also shown in the figure). Figure 2b shows the typical HRTEM images of the TiO_2 nanostructure and the inset shows a selective-area electronic diffraction pattern. It reveals that TiO_2 has a rutile crystal structure. The lattice spacing is about 3.2 \AA between adjacent lattice planes of the TiO_2 needles, corresponding to the distance between (110) crystal planes of the rutile phase. The dispersion of TiO_2 nanoneedles in MEH-PPV was further analyzed by TEM. The samples for TEM study were prepared by directly coating the TiO_2 /MEH-PPV solution on a C-Cu grid. The TEM images of TiO_2 /MEH-PPV containing different amounts of TiO_2 are shown in Figure 3a-c, and they show that the TiO_2 nanoneedles were well dispersed in MEH-PPV. The percolation network geometry of TiO_2 increases, while the percentage of incorporated TiO_2 in the composites increases. The enlarged image shown in Figure 3d reveals that the TiO_2 nanoneedles formed a percolation network geometry in MEH-PPV. These TiO_2 nanoneedles are about 100 nm in length and 30 nm in width, terminating with a sharp pinnacle.

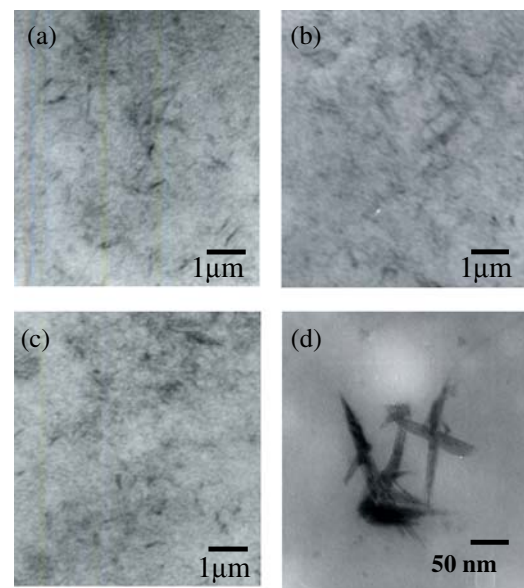


Figure 3. TEM image of TiO_2 /MEH-PPV composites containing (a) 1 wt% TiO_2 , (b) 3 wt% TiO_2 , and (c) 5 wt% TiO_2 . (d) TEM image (zoom in) of the percolation network of TiO_2 nanoneedles in MEH-PPV.

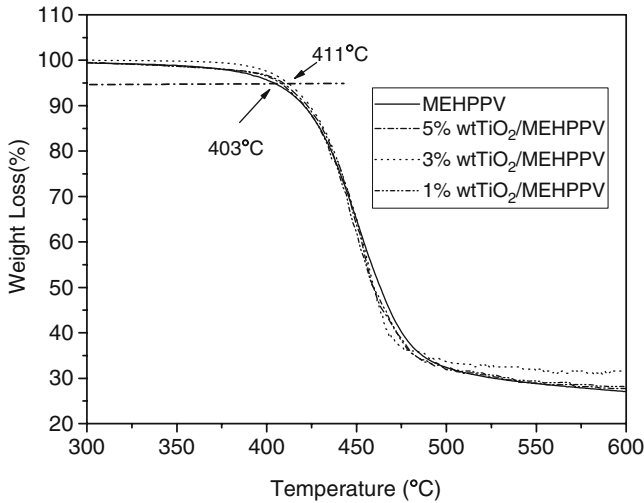


Figure 4. Thermal gravimetric properties of MEH-PPV and 1, 3, and 5 wt% TiO_2 /MEH-PPV composites.

The thermal gravimetric properties of TiO_2 /MEH-PPV composites are shown in Figure 4. The 5% weight loss degradation temperature of 5 wt% TiO_2 /MEH-PPV composites is 8 °C higher than that of MEH-PPV. Figure 5 is a differential scanning calorimetry (DSC) thermogram of MEH-PPV and 5 wt% TiO_2 /MEH-PPV composite. The glass-transition temperatures are 63 and 65 °C for MEH-PPV and 5 wt% TiO_2 /MEH-PPV composite, respectively. There is also a broad endotherm spanning the temperature range 150–260 °C. The broad endotherm should be the nematic-to-isotropic transition of MEH-PPV [37–39]. The endotherm peak of 5 wt% TiO_2 /MEH-PPV is larger than that of pure MEH-PPV (0.68 vs 0.53 J/g). This could be caused by the hydrogen bond that is formed by the O atom attached to the phenyl group of the main chain of MEH-PPV with the dangling hydroxyl groups on the TiO_2 needle surface. It further indicates that TiO_2 nanoneedles could induce the long-range order of MEH-PPV and therefore cause the endotherm of the crystal phase transition of MEH-PPV to increase. Figure 6 displays the XRD curve of

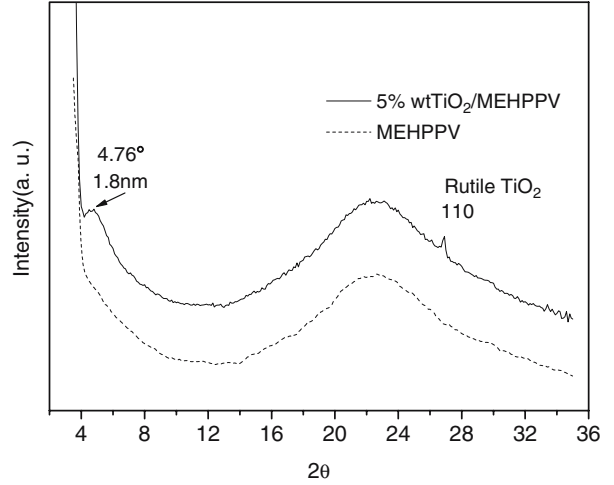


Figure 6. X-ray diffraction curves of MEH-PPV and 5 wt% TiO_2 /MEH-PPV composite.

MEH-PPV and 5 wt% TiO_2 /MEH-PPV composite. The clear peak in the vicinity of $2\theta = 4.7^\circ$ with a d spacing value of 1.8 nm reveals that MEH-PPV films containing TiO_2 had long-range nanoscale modulation. This result is in agreement with the result of DSC.

Figure 7 shows PL spectra of MEH-PPV composites film containing different amounts of TiO_2 nanoneedles. The samples were excited by a xenon lamp at 480 nm. The thicknesses of these films were determined by atomic force microscopy to be about approximately 240 nm. The PL spectra of the nanocomposite films exhibit a similar pattern as that of pure MEH-PPV, with a slightly decreased peak intensity at 588 nm. There is a 7% decrease in the luminescence intensity at 588 nm for 5 wt% TiO_2 in MEH-PPV. This indicates that the quenching of the luminescence is limited when TiO_2 needles are added because of the limited surface area of TiO_2 nanoneedles.

To reveal the electrical properties of TiO_2 /MEH-PPV composites, the I – V characteristics of ITO/MEH-PPV: TiO_2 /Al were explored. Figure 8a shows the results for

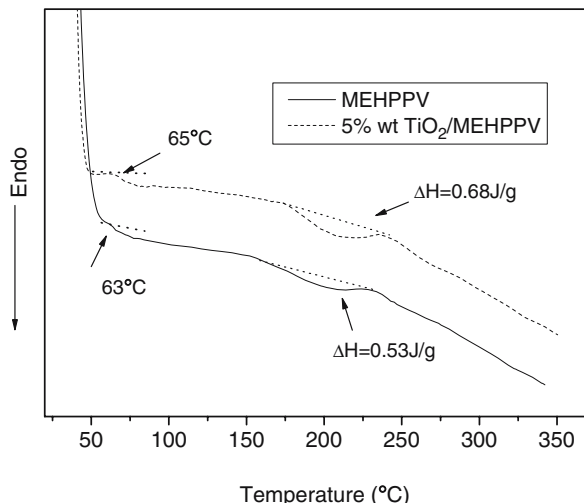


Figure 5. Differential scanning calorimetry thermogram of MEH-PPV and 5 wt% TiO_2 /MEH-PPV composite.

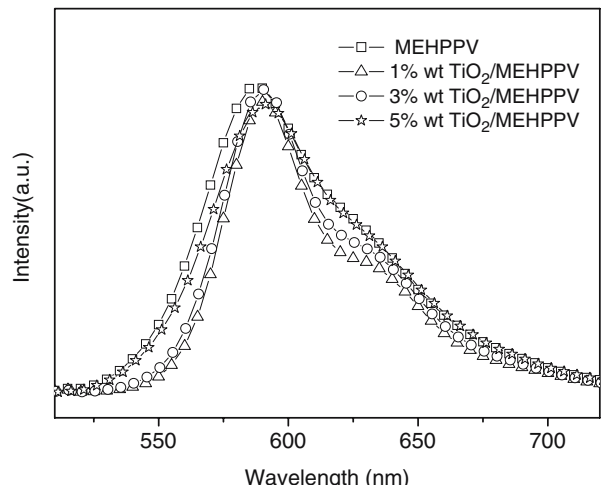


Figure 7. Photoluminescence of MEH-PPV and TiO_2 /MEH-PPV composite films.

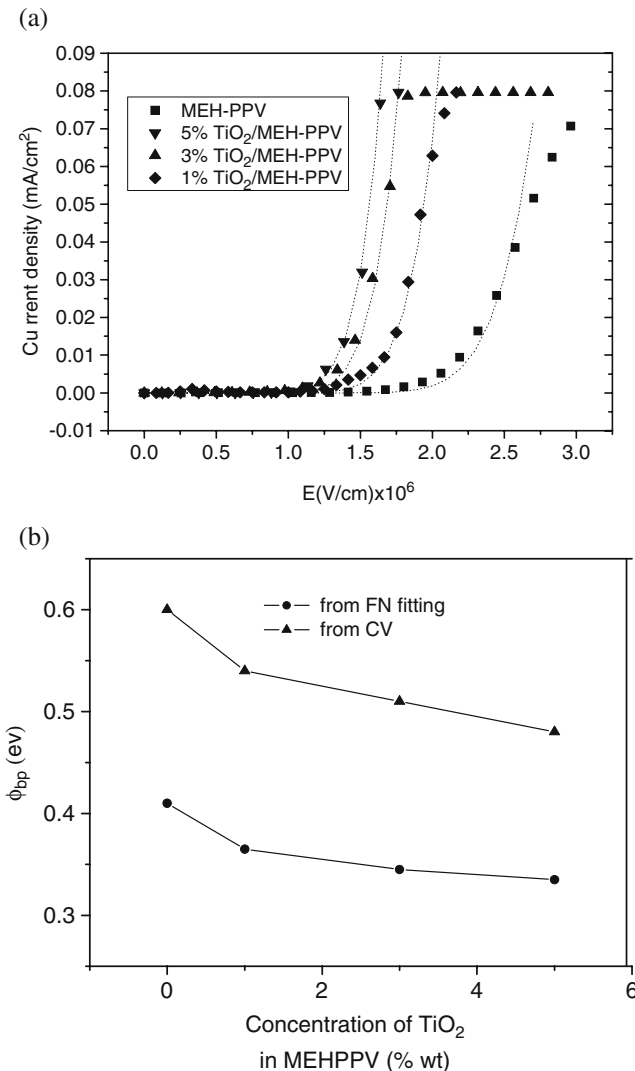


Figure 8. (a) Model and experimental J - E curves of MEH-PPV and TiO₂ nanoneedles/MEH-PPV composites. The dotted line is a fit to the data. (b) Hole barrier height from cyclic voltammetry (CV) and Fowler–Nordheim (FN) fitting vs the amount of TiO₂ incorporated in MEH-PPV.

the MEH-PPV and TiO₂/MEH-PPV composites. The turn-on voltages for the devices were observed to decrease as the amount of incorporated TiO₂ nanoneedles increased. To study the charge injection mechanism under direct current bias, we considered Richardson–Schottky thermionic emission and Fowler–Nordheim (FN) tunneling

models. Under forward bias, at high applied fields ($>5 \times 10^5 \text{ V}/\text{cm}$), the J – E characteristics are determined by FN tunneling (Equation 1) of both electrons and holes through contact barriers arising from the band offset between the polymer and the electrodes. Furthermore, at low fields the tunneling model was found not to be applicable to the experimental J – E characteristics, which has been attributed to the contribution of thermionic emission to the current and to band-bending effects at the interface. According to the model, the tunneling current density J at a particular applied electric field E can be expressed as [40, 41]

$$J_{tun} = ACE^2 \exp\left(-\frac{8\pi\sqrt{2em\phi_{bp}^3}}{3hE}\right), \quad (1)$$

with $C = \frac{3e^2}{8\pi h\phi_{bp}}$.

Here, e is the elementary charge, m is the effective hole mass, h is Planck's constant, and ϕ_{bp} is the hole barrier height. A is a dimensionless parameter and is set equal to 5.3×10^{-8} [40]. The measured I – E characteristic curves were fitted to the FN equation with the fitting parameter ϕ_{bp} . We find that as the weight percentage of TiO₂ is increased, ϕ_{bp} decreases. The highest occupied molecular orbital (HOMO) and lowest unoccupied molecular orbital (LUMO) energy levels of MEH-PPV are reported to be 5.4 eV [42] and 3.0 eV [43], respectively, yielding a bandgap (E_g) of 2.4 eV. The workfunction of Al is 4.3 eV, which results in a 1.3-eV barrier to electron injection (ϕ_{bn}) at the cathode of the light-emitting diode. The energy of the HOMO level can be estimated from the oxidation potential measured with CV. Table 1 summarizes the results: The hole barrier height is estimated from either a CV measurement or FN fitting of the J – E curves. However, the energy of the LUMO level is less reliably determined from the CV measurement because of the water content of the materials used. Figure 8b presents a comparison of hole barrier height, determined from CV measurements and FN fitting results as a function of the amount of TiO₂ in MEH-PPV. It clearly shows the same trend: The hole barrier height decreases as the amount of the TiO₂ nanoneedles in MEH-PPV is increased. Hole barrier height decrease could be caused by the interchain aggregation and partial crystals of MEH-PPV between the interface of the electrode and

Table 1. Hole barrier height estimated from the Fowler–Nordheim (FN) equation and from cyclic voltammetry (CV) measurements and hole mobility estimated from linear fits of $\ln(J/E^2)$ vs \sqrt{E}

	ϕ_{bp} (eV) ^a	HOMO from CV (eV)	Hole barrier ^b height (eV)	Hole mobility μ_0 ($\times 10^{-7} \text{ cm}^2/\text{V S}^{-1}$)
MEH-PPV	0.41 ± 0.01	-5.30 ± 0.11	0.6 ± 0.11	2.10
1 wt% TiO ₂ in MEH-PPV	0.36 ± 0.01	-5.24 ± 0.07	0.54 ± 0.07	3.56
3 wt% TiO ₂ in MEH-PPV	0.34 ± 0.02	-5.21 ± 0.09	0.51 ± 0.09	5.68
5 wt% TiO ₂ in MEH-PPV	0.32 ± 0.03	-5.18 ± 0.10	0.48 ± 0.10	6.21

The work function of indium tin oxide was set equal to -4.7 eV .

MEH-PPV poly(2-methoxy-5-(2'-ethylhexyloxy)-1,4-phenylene vinylene).

^aThe hole barrier height, ϕ_{bp} , estimated from the FN fitting of the measured J – E characteristic curves.

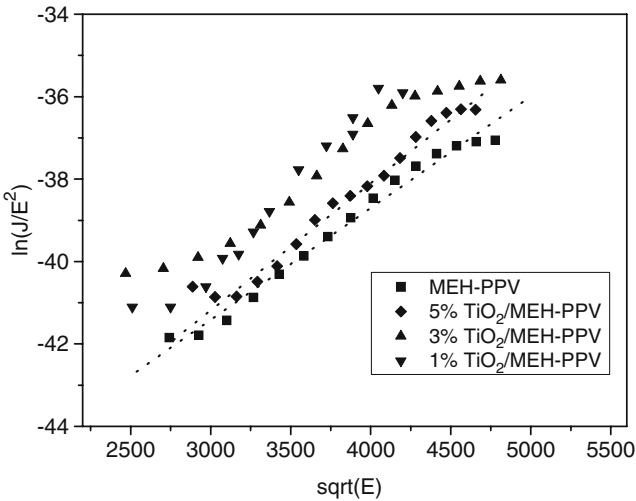


Figure 9. $\ln(J/E^2)$ vs \sqrt{E} gives the field-independent mobility term μ_0 .

the composite interface. Hole mobility in MEH-PPV could be determined by taking $J-E$ curves and fitting the data to a spacecharge limited form for a single carrier, as derived by Mott and Gurney [44, 45].

$$J = 9/8\epsilon\mu E^2/L, \quad (2)$$

where E is the electric field across the device, L is the polymer thickness, and a value of $\epsilon = 3.1 \times 10^{-11} C^2/(Nm^2)$ is assumed for the polymer [44]. A Poole-Frenkel-like form is assumed for the mobility:

$$\mu = \mu_0 \exp(0.89\gamma\sqrt{E}). \quad (3)$$

The linear fits of $\ln(J/E^2)$ vs \sqrt{E} give the field-independent mobility term μ_0 , and are given in Figure 9 and the data are collected in Table 1. The hole mobility in MEH-PPV shows a threefold enhancement when 5 wt% TiO_2 nanoneedles are incorporated in MEH-PPV. The improvement in polymer hole mobility caused by a partial crystallization of MEH-PPV agrees with a previous study [44]. Although $\mu_{TiO_2} \gg \mu_{PPV}$ for both electron and holes ($\mu_{n,TiO_2} = 0.1 - 1 cm^2/V/S$ and μ_{p,TiO_2} is at least an order of magnitude lower [32]; $\mu_{p,PPV} < 10^{-4} cm^2/V/S$ and $\mu_{e,PPV}$ is at least 2 orders of magnitude lower [46]), the hole transfer to the

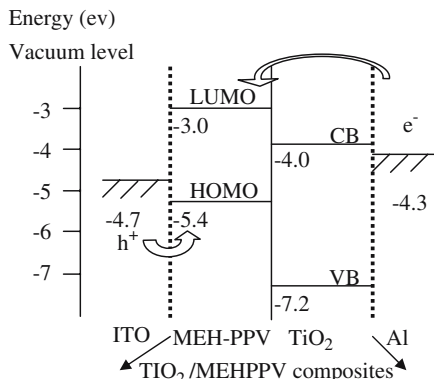


Figure 10. Energy diagram for TiO_2 and MEH-PPV and work functions for Al and indium tin oxide (ITO).

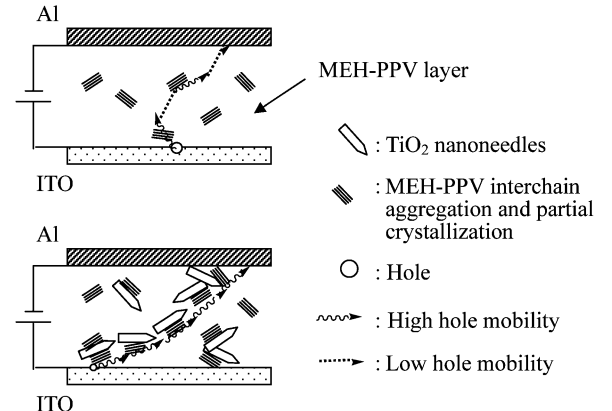


Figure 11. Schematic drawing of hole traveling path in a TiO_2 /MEH-PPV composite device.

TiO_2 nanocrystals is energetically unfavorable (Figure 10). Therefore, the hole would transfer favorably in partial crystallization of MEH-PPV, which formed a percolation network geometry. The scheme is shown in Figure 11. Figure 12 shows EL spectra of pure MEH-PPV and 1, 3, and 5 wt% TiO_2 /MEH-PPV composites at an applied electric field $1.8 \times 10^6 V/cm$. The thicknesses of these films are approximately 240 nm. The normalized integrated area of the EL spectrum as a function of TiO_2 weight percentage in MEH-PPV is shown in the inset in Figure 12. The EL intensity of the 590-nm peak from the thin-film device consisting of 5 wt% TiO_2 displays a 3.7-fold increase. EL spectra of the nanocomposite films exhibit a similar profile as that of pure MEH-PPV. A 2.8-fold increase in the normalized integrated area of EL was achieved with MEH-PPV containing 5 wt% TiO_2 nanoneedles. The decrease in turn-on voltage and, therefore, hole barrier height and mobility is a reflection of improved hole injection efficiency. Both the significant reduction in diode turn-on voltage and the increase in current efficiency lead to an obvious improvement in the power efficiency of MEH-PPV light-emitting diodes with the addition of TiO_2 nanoneedles.

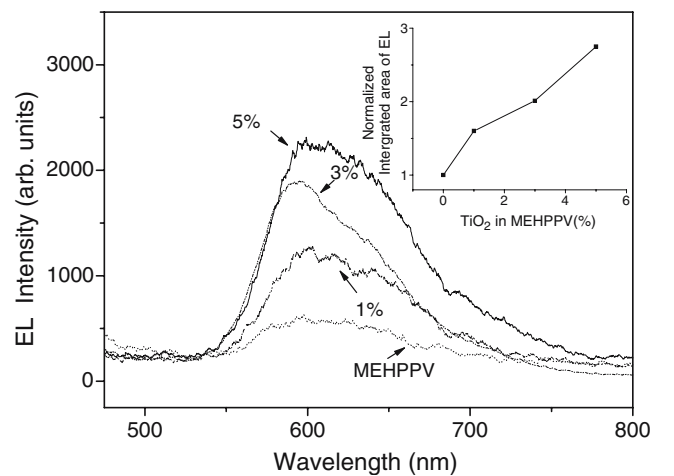


Figure 12. Electroluminescence (EL) of MEH-PPV and TiO_2 /MEH-PPV composite films. The normalized integrated area of EL vs TiO_2 weight percentage in MEH-PPV is shown in the inset.

Conclusion

In summary, we find that EL of MEH-PPV thin films can be enhanced via addition of TiO₂ nanoneedles. A 2.8-fold enhancement in the normalized integrated area of EL was achieved with 5 wt% TiO₂ nanoneedles in MEH-PPV. The enhancement of EL may be due to the decrease in hole barrier height and the increase in hole mobility. The hole barrier height (ϕ_{bn}), estimated from $J-E$ characteristic curves, was found to decrease from 0.41 to 0.32 eV as the amount of incorporated TiO₂ nanoneedles increased from 0 to 5%. The hole mobility was found to increase as TiO₂ nanoneedles were incorporated in MEH-PPV.

Acknowledgments

We appreciate the financial support of the National Science Council, Taiwan, through project NSC 92-2120-M-009-009.

References

1. N. S. Sariciftci, L. Smilowitz, A. J. Heeger and F. Wudl, *Science*, **258**, 1474 (1992).
2. G. Yu, J. Gao, J. C. Hummelen, F. Wudl and A. J. Heeger, *Science*, **270**, 1789 (1995).
3. K. S. Narayan and T. B. Singh, *Appl. Phys. Lett.*, **74**, 3456 (1999).
4. B. van der Zanden and A. Goossens, *J. Appl. Phys.*, **10**, 6959 (2003).
5. P. A. van Hal, M. P. T. Christiaans, M. M. Wienk, J. M. Kroon and R. A. J. Janssen, *J. Phys. Chem., B*, **103**, 4352 (1999).
6. Q. Fan, B. McQuillin, D. D. C. Bradley, S. Whitelegg and A. B. Seddon, *Chem. Phys. Lett.*, **347**, 325 (2001).
7. M. P. T. Christiaans, M. M. Wienk, P. A. van Hal, J. M. Kroon and R. A. J. Janssen, *Synth. Met.*, **101**, 265 (1999).
8. S. H. Jin, M. S. Jang and H. S. Suh, *Chem. Mater.*, **14**, 643 (2002).
9. D. Y. Kim, S. K. Lee, J. L. Kim, J. K. Kim, H. Lee, H. N. Cho, S. I. Hong and C. Y. Kim, *Synth. Met.*, **121**, 1707 (2001).
10. T. Q. Nguyen, I. B. Martini, J. Liu and B. J. Schwartz, *J. Phys. Chem., B*, **104**, 237 (2000).
11. G. Padmanaban and S. Ramakrishnan, *Synth. Met.*, **119**, 533 (2001).
12. G. Padmanaban and S. Ramakrishnan, *J. Am. Chem. Soc.*, **122**, 2244 (2000).
13. X. Deng, L. Zheng, C. Yang, Y. Li, G. Yu and Y. Cao, *J. Phys. Chem., B*, **108**, 3451 (2004).
14. S. Xiao, M. Nguyen, X. Gong, Y. Cao, H. Wu, D. Moses and A. J. Heeger, *Adv. Funct. Mater.*, **13**, 25 (2003).
15. A. Petrella, M. Tamborra, P. D. Cozzoli, M. L. Curri, M. Striccoli, P. Cosma, G. M. Farinola, F. Babudri, F. Naso and A. Agostiano, *Thin Solid Films*, **451-452**, 64 (2004).
16. Y. K. Kim, K. Y. Lee, O. K. Kwon, D. M. Shin, B. C. Sohn and J. H. Choi, *Synth. Met.*, **111-112**, 207 (2000).
17. J. C. Scott and P. J. Brock, *Appl. Phys. Lett.*, **71**, 1145 (1997).
18. Y. H. Kim, D. Kim, S. C. Jeoung, J. Y. Han, M. S. Jang and H. K. Shim, *Chem. Mater.*, **14**, 643 (2001).
19. N. Tessler, V. Medvedev, M. Kazes, S. Kan and U. Banin, *Science*, **295**, 1506 (2002).
20. J. Cheng, S. Wang, X. Y. Li, Y. J. Yan, S. Yang, C. L. Yang, J. N. Wang and W. K. Ge, *Chem. Phys. Lett.*, **333**, 375 (2001).
21. F. Hide, B. J. Schwartz, M. A. Diaz-Garcia and A. J. Heeger, *Chem. Phys. Lett.*, **256**, 424 (1996).
22. B. O. Dabbousi, M. G. Bawendi, O. Onitsuka and M. F. Rubner, *Appl. Phys. Lett.*, **66**, 1316 (1995).
23. J. S. Salafsky, W. H. Lubberhuizen and R. E. I. Schropp, *Chem. Phys. Lett.*, **290**, 297 (1998).
24. W. U. Huynh, J. J. Dittmer and A. P. Alivisatos, *Science*, **295**, 2425 (2002).
25. D. J. Milliron, A. P. Alivisatos, C. Pitois, C. Edder and J. M. J. Fréchet, *Adv. Mater.*, **15**, 58 (2003).
26. L. Bakueva, S. Musikhin, M. A. Hines, T. W. F. Chang, M. Tzolov, G. D. Scholes and E. H. Sargent, *Appl. Phys. Lett.*, **82**, 2895 (2003).
27. H. Matoussi, L. H. Radzilowski, B. O. Dabbousi, E. L. Thomas, M. G. Bawendi and M. F. Rubner, *J. Appl. Phys.*, **83**, 7698 (1998).
28. M. C. Schlamp, X. Peng and A. P. Alivisatos, *J. Appl. Phys.*, **82**, 5837 (1997).
29. N. C. Greenham, X. Peng and A. P. Alivisatos, *Phys. Rev., B*, **54**, 17628 (1996).
30. C. Y. Kwong, W. C. H. Choy, A. B. Djurisic, P. C. Chui, K. W. Cheng and W. K. Chan, *Nanotechnology*, **15**, 1156 (2004).
31. W. I. Sha, C. H. Liu and R. R. Alfano, *Opt. Lett.*, **19**, 1922 (1995).
32. H. O. Finklea, in: *Semiconductor Electrodes*, H. O. Finklea, Ed., Elsevier, New York, 1988, p. 52.
33. K. D. Benkstein, N. Kopidakis, J. Van de Lagemaat and A. J. Frank, *J. Phys. Chem., B*, **107**, 7759 (2003).
34. B. Sun, E. Marx and N. C. Greenham, *Nano Lett.*, **3**, 961 (2003).
35. M. Adachi, Y. Murata, J. Takao, J. Jiu, M. Sakamoto and F. Wang, *J. Am. Chem. Sci.*, **126**, 14943 (2004).
36. C. C. Weng, K. F. Hsu and K. H. Wei, *Chem. Mater.*, **16**, 4080 (2004).
37. S. H. Chen, A. C. Su, H. L. Chou, K. Y. Peng and S. A. Chen, *Macromolecules*, **37**, 167 (2004).
38. S. H. Chen, A. C. Su, C. S. Chang, H. L. Chen, D. L. Ho, C. S. Tsao, K. Y. Peng and S. A. Chen, *Langmuir*, **20**, 8909 (2004).
39. S. H. Chen, A. C. Su, Y. F. Huang, C. H. Su, G. Y. Peng and S. A. Chen, *Macromolecules*, **35**, 4229 (2002).
40. S. J. Martin, J. M. Lupton, I. D. W. Samuel and A. B. Walker, *J. Phys. Condens. Matter.*, **14**, 9925 (2002).
41. Y. Kawabe, M. M. Morrell, G. E. Jabbour, S. E. Shahen and B. Kippelen, *J. Appl. Phys.*, **84**, 5306 (1998).
42. L. Bozano, S. A. Carter, J. C. Scott, G. G. Malliaras and P. J. Brock, *Appl. Phys. Lett.*, **74**, 1132 (1999).
43. I. H. Campbell, T. W. Hagler, D. L. Smith and J. P. Ferraris, *Phys. Rev. Lett.*, **76**, 1900 (1996).
44. A. J. Breeze, Z. Schlesinger and S. A. Carter, *Phys. Rev., B*, **64**, 125205 (2004).
45. N. F. Mott and R. W. Gurney, *Electronic Processes in Ionic Crystals*, Oxford University Press, London, 1948.
46. N. C. Greenham and R. H. Friend, *Solid State Phys.*, **49**, 1 (1995).